Journal of Alloys and Compounds 509 (2011) 8460–8468

Contents lists available at ScienceDirect

Journal of Alloys and Compounds

journal homepage: www.elsevier.com/locate/jallcom

Synthesis and characteristics of poly(3-pyrrol-1-ylpropanoic acid) (PPyAA)–Fe_3O_4 nanocomposite

E. Karaoğlu[a], A. Baykal[a,*], H. Deligöz[b], M. Şenel[a], H. Sözeri[c], M.S. Toprak[d]

[a] Department of Chemistry, Fatih University, 34500 Buykcekmece-Istanbul, Turkey
[b] Chemical Engineering Department, Istanbul University, 34320 Avcılar-Istanbul, Turkey
[c] TUBITAK-UME, National Metrology Institute, PO Box 54, 41470 Gebze-Kocaeli, Turkey
[d] Functional Materials Division, Royal Institute of Technology – KTH, SE16440 Stockholm, Sweden

ARTICLE INFO

Article history:
Received 4 March 2011
Received in revised form 31 May 2011
Accepted 1 June 2011
Available online 12 June 2011

Keywords:
Conducting polymer
Fe_3O_4
Nanocomposite
Magnetization
Dielectric properties
a.c./d.c. conductivity

ABSTRACT

Poly(3-pyrrol-1-ylpropanoic acid) (PPyAA)–Fe_3O_4 nanocomposite was successfully synthesized by an in situ polymerization of 1-(2-carboxyethyl) pyrrole in the presence of synthesized Fe_3O_4 nanoparticles. Evaluation of structural, morphological, electrical and magnetic properties of the nanocomposite was performed by XRD, FT-IR, TEM, TGA, magnetization and conductivity measurements, respectively. XRD analysis reveals the inorganic phase as Fe_3O_4 and TGA shows about 90 wt% loading of Fe_3O_4 in the nanocomposite. FT-IR analysis indicates a successful conjugation of Fe_3O_4 particles with polypyrrole acetic acid. Magnetization measurements show that polypyrrole acetic acid coating decreases the saturation magnetization of Fe_3O_4 significantly. This reduction has been explained by the pinning of the surface spins by the possible adsorption of non-magnetic ions during the polymerization process. The conductivity and dielectric permittivity measurements strongly depend on the thermally activated polarization mechanism and thermal transition of PPyAA in the nanocomposite structure. Large value of dielectric permittivity (ε') of the nanocomposite at lower frequency is attributed to the predominance of species like Fe^{2+} ions and grain boundary defects (interfacial polarization).

1. Introduction

In the last decade, many authors became interested in magnetic nanopowder-reinforced polymer composites because magnetic nanoparticles have shown great potential for applications, including aircraft, spacecraft, magnetic hard disks, and the magnetic bars of credit card. These applications can take advantage of both the magnetic properties and wear properties of these compositions [1,2].

Conducting polymers have attracted considerable attention for their potential applications in various fields such as electromagnetic interface (EMI) shielding [3], rechargeable batteries [4], electrodes and sensors [5], corrosion protection coatings [6], and microwave absorption [7]. Recently, many efforts have been devoted to fabricating magnetic and conductive composites with core–shell structure.

Major advancements are achieved in synthesis and characterization of conducting polymeric matrices with embedded magnetic nanoparticles which constitute an important class of nanostructures [8–11]. These nanostructures/nanocomposites exhibit novel physical properties owing to the nanoscale confinement of the magnetic constituents, abundance of interfaces, and extent of dispersion of fine particles within nonmagnetic polymer matrices.

Since nanocomposites often exhibit improved chemical and physical properties over their single-component counterparts, in order to realize the full potential of technological applications of inorganic nanomaterials and conducting polymers, a large number of articles have been published reporting on the polymeric nanocomposites i.e., salicylic acid, aminoacids, polypyrrole composites containing Fe_3O_4 nanoparticles [12–20].

Recently, many studies of magnetic, electrical and ferromagnetic properties of conducting polymer composites have received increasing attention, and studies on this kind of composites have become one of the most active and promising research areas [21–23]. What makes conducting polymer composites so attractive is their potential applications in batteries [24], electro-chemical display devices [25], molecular electronics [3], electrical–magnetic shields, and microwave-absorbing materials [26]. It is well-known that conducting polymers can effectively shield electromagnetic waves generated from an electric source, whereas electromagnetic waves from a magnetic source can be effectively shielded only by magnetic materials. Thus, the incorporation of magnetic constituents and conducting polymeric materials into multifunctional composites opens new possibilities for the achievement

* Corresponding author. Tel.: +90 212 866 33 00x2070; fax: +90 212 866 34 02.
E-mail address: hbaykal@fatih.edu.tr (A. Baykal).

0925-8388/$ – see front matter © 2011 Elsevier B.V. All rights reserved.
doi:10.1016/j.jallcom.2011.06.002

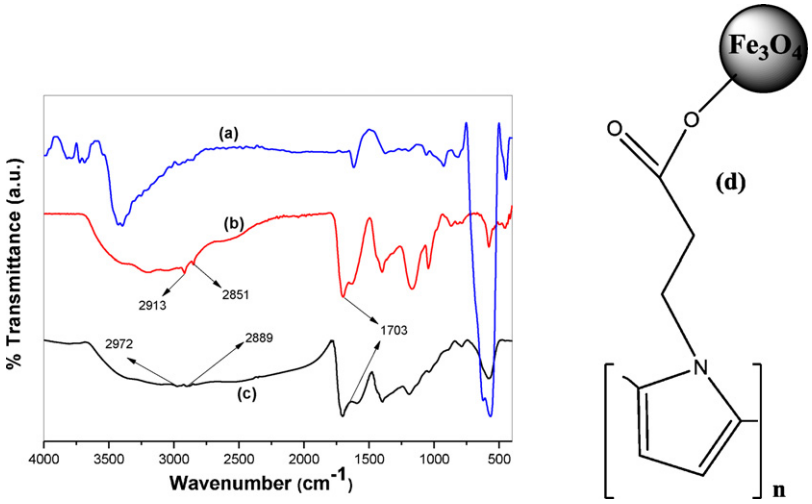

Fig. 1. FT-IR spectra of (a) Fe_3O_4, (b) PPyAA–Fe_3O_4 nanocomposite, (c) PPyAA and (d) suggested linkage of PPyAA acid to iron oxide surface.

of good shielding effectiveness for various electromagnetic sources [27,28].

In this work, we reported on the synthesis of Fe_3O_4 and its composite formation with conducting polymer poly(3-pyrrol-1-ylpropanoic acid) (PPyAA). This is the first report on the synthesis of such nanocomposite materials. Its magnetic and electrical properties were evaluated and detailed results are presented.

2. Experimental

2.1. Chemicals

The raw materials were analytical grade of 1-(2-cyanoethyl) pyrrole (Py-CN), KOH, HCl, APS, $FeCl_3{\cdot}2H_2O$, $FeCl_2{\cdot}4H_2O$ (Merck) and were used as-received, without further purification.

2.2. Chemicals and instrumentation

X-ray powder diffraction (XRD) analysis was conducted on a Rigaku Smart Lab operated at 40 kV and 35 mA using Cu K_α radiation.

Fourier transform infrared (FT-IR) spectra were recorded in transmission mode with a Perkin Elmer BX FT-IR infrared spectrometer. The powder samples were ground with KBr and compressed into a pellet. FT-IR spectra is in the range of 4000–400 cm^{-1}.

Transmission electron microscopy (TEM) analysis was performed using FEI Tecnai G2 Sphera microscope. A drop of diluted sample in alcohol was dripped on a TEM grid and dried prior to insertion to TEM column.

The thermal stability was determined by thermogravimetric analysis (TGA, Perkin Elmer Instruments model, STA 6000). The TGA thermograms were recorded for 5 mg of powder sample at a heating rate of 10 °C/min in the temperature range of 30–800 °C under nitrogen atmosphere.

VSM measurements were performed by using a Quantum Design Vibrating sample magnetometer (QD-VSM). The sample was measured between ±10 kOe at room temperature (25 °C).

The electrical conductivity of the PPyAA–Fe_3O_4 nanocomposite was studied in the temperature range of 20–120 °C with a heating rate of 10 °C/s. The sample was used in the form of circular pellets of 13 mm diameter and 3 mm thickness. The pellets (both nanocomposite and pristine) were sandwiched between gold electrodes and the conductivities were measured using Novocontrol dielectric impedance analyzer in the frequency range 1 Hz–3 MHz, respectively. The temperature (between −100 and 250 °C) was controlled with a Novocool Cryosystem.

2.3. Procedure

2.3.1. Synthesis of poly(3-pyrrol-1-ylpropanoic acid) (PPyAA)

In a typical procedure, a certain amount of 1-(2-carboxyethyl) pyrrole monomer was added to 35 ml of 0.5 M HCl solution, then sonicated in an ultrasonic bath for 120 min at 0 °C. Then 3.5 g of APS in 20 ml of 0.5 M HCl solution was added drop-wise to the above mixture. The composites were obtained by filtering and washing the reaction mixture with deionized water and ethanol, afterwards dried under vacuum at 50 °C for 24 h.

2.3.2. Synthesis of PPyAA–Fe_3O_4 nanocomposite

The stoichiometric amount of Fe(III) and Fe(II) salts was dissolved in minimum amount water and then solution was kept at a constant temperature of 40 °C for 15 min under vigorous stirring.

Then a certain amount of prepared PPyAA and solution of sodium hydroxide was added to the above mixture till the pH was raised to 11 at which a black suspension was formed. This suspension was then refluxed at 80 °C for 6 h, under vigorous stirring and Ar gas. PPyAA–Fe_3O_4 nanocomposite was separated from the aqueous solution by magnetic decantation, washed with distilled water several times and then dried in an oven overnight.

3. Results and discussion

3.1. FT-IR analysis

Fig. 1 shows the typical FT-IR spectrum of Fe_3O_4 NPs, PPyAA–Fe_3O_4 nanocomposite, PPyAA and suggested linkage of PPyAA to iron oxide surface respectively. As can be seen from Fig. 1(a), magnetite powder has metal-oxygen band, ν_1, observed at 590 cm^{-1} which corresponds to intrinsic stretching vibrations of the metal at tetrahedral site ($Fe_{tetra} \leftrightarrow O$), whereas metal-oxygen band observed at 445 cm^{-1}, ν_2, is assigned to octahedral-metal stretching ($Fe_{octa} \leftrightarrow O$) [29]. In the spectrum for PPyAA presented in Fig. 1(b), two sharp bands at 2924 cm^{-1} and 2854 cm^{-1} were

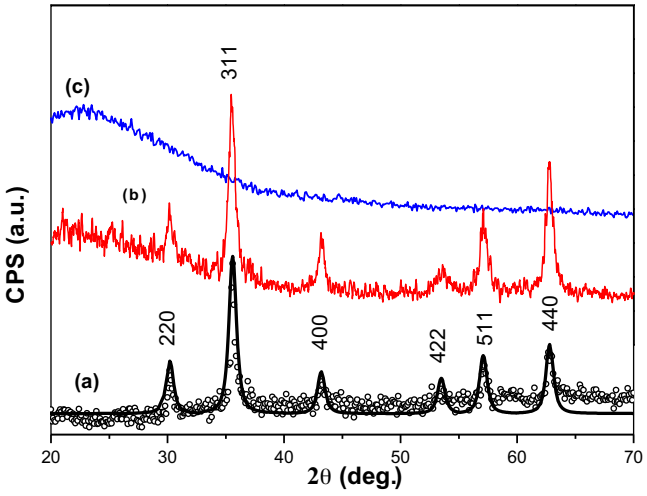

Fig. 2. XRD powder pattern of (a) PPyAA–Fe_3O_4 nanocomposite, (b) pure magnetite and (c) PPyAA.

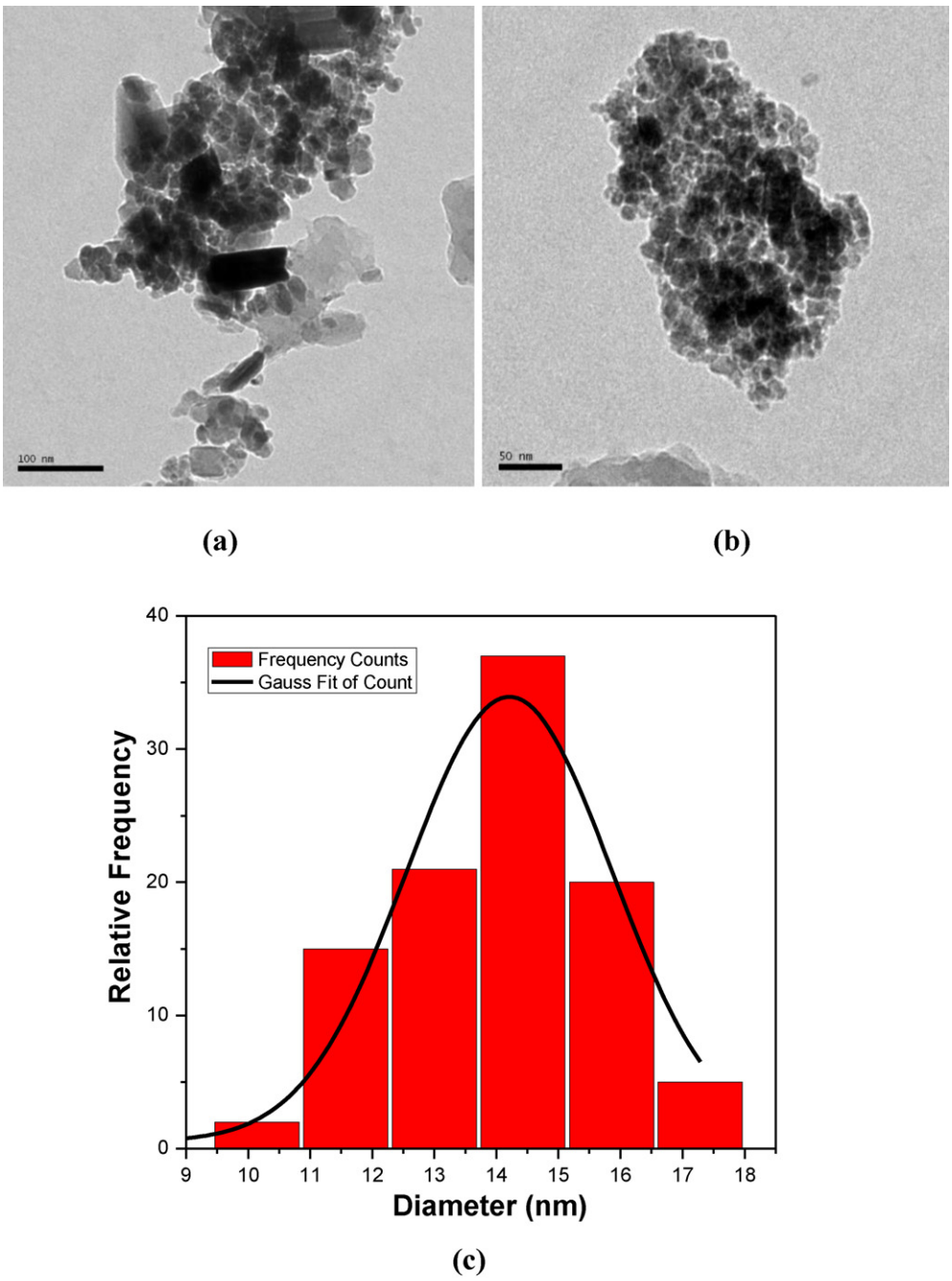

Fig. 3. (a and b) TEM micrographs of PPyAA–Fe_3O_4 nanocomposite at different magnifications and (c) histogram representing the size distribution of Fe_3O_4 NPs in the nanocomposite.

attributed to asymmetric and symmetric CH_2 stretching vibrations, respectively. In the spectrum of PPyAA–Fe_3O_4 nanocomposite, presented in Fig. 1(c), the asymmetric and symmetric CH_2 stretching vibrations shifted to 2922 and 2852 cm^{-1}, respectively. For both PPyAA and nanocomposite, the intense peak at 1700 cm^{-1} was derived from the existence of the C=O stretching band [30,31]. On the basis, as was argued by Bronswijk et al. [32,33], when the carboxylate group is directly involved in adsorption it is possible to discriminate between monodentate, bidentate chelating, and bidentate bridging structures. In the monodentate structure, the higher of the two carboxylate frequencies occurs at around 1680 cm^{-1} and is indicative of significant C=O character. Therefore, the presence of C=O peak in the FT-IR spectrum of nanocomposite indicates the monodentate chelation as shown in Fig. 1(d).

3.2. XRD analysis

Crystalline phases that are present in the final material were identified by XRD. Amorphous structure of PPyAA is shown in Fig. 2(c). The resultant pattern is given in Fig. 2(a) which indicates that the product is magnetite, Fe_3O_4 (Fig. 2(b)). All of the observed diffraction peaks are indexed by the cubic structure of Fe_3O_4 (JCPDS no. 19-629). The broadening of the diffraction peaks rather indicates nano-crystalline features of the product. To determine the crystallite size of the sample, the XRD profile was fitted according to Eq. (1) in Wejrzanowski et al. [34] and Pielaszek [35] which allows the estimation of average crystallite size and its standard deviation from XRD. The experimental line profile, shown in Fig. 2, was fitted for six peaks with $h\,k\,l$ indices of (2 2 0), (3 1 1), (4 0 0),

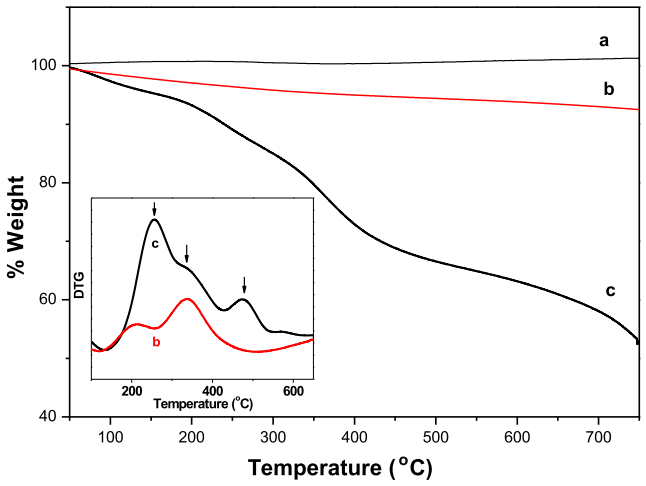

Fig. 4. TGA thermograms of (a) Fe_3O_4 nanoparticles, (b) PPyAA–Fe_3O_4 nanocomposite and (c) PPyAA.

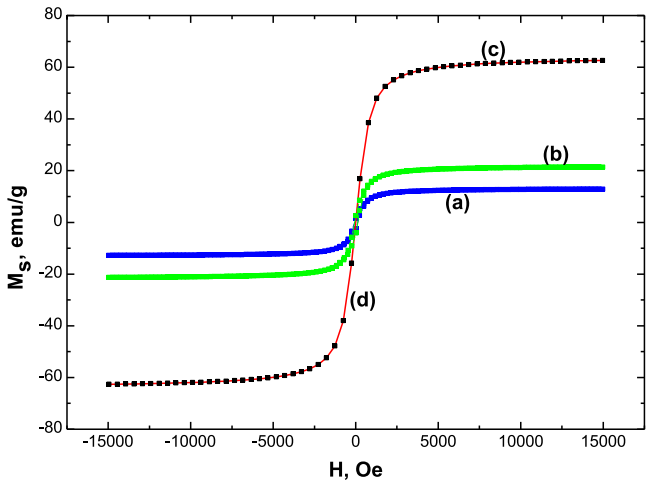

Fig. 5. *M–H* hysteresis curves of (a) PPyAA–Fe_3O_4 nanocomposite, (b) PPyAA–Fe_3O_4 with normalized mass, (c) bulk magnetite (■) measured at room temperature and (d) Langevin Fit (-).

(4 2 2), (5 1 1), and (4 4 0). The calculated average crystallite size, D_{XRD}, is 11 ± 4 nm.

3.3. TEM analysis

TEM micrographs of PPyAA–Fe_3O_4 nanocomposite with different magnifications are shown in Fig. 3(a) and (b). The size distribution diagram is presented in Fig. 3(c). Fe_3O_4 particles are observed to have spherical morphology and are agglomerated due to the polymer coating. Size distribution histogram is obtained by measuring at least 150 nanoparticles and is fitted by using a log-normal function [36]. An average size, $D_{TEM/log\text{-}normal}$, of 14 ± 3 nm was obtained for magnetite nanoparticles. Crystallite size obtained from XRD line profile fitting versus particle size estimated from TEM is very similar.

3.4. Thermal analysis

Thermal gravimetric analysis of iron oxide nanoparticles, PPyAA and PPyAA–Fe_3O_4 nanocomposite was performed to investigate the stability of composite and to confirm the interaction between Fe_3O_4 nanoparticles and PPyAA. No considerable weight loss was observed for Fe_3O_4 NPs (Fig. 4(a)). PPyAA exhibits three step decomposition; the first one around 230 °C due to the removal of adsorbed water with ~10 wt% loss. The second step decomposition starts from 320 °C and goes up to 400 °C (inset graph) with about 30% loss (Fig. 4(c)). The third step was the continuation of decomposition of PPyAA which was not completed in the working temperature range.

Thermogram of PPyAA–Fe_3O_4 nanocomposite is shown in Fig. 4(b) with a significant weight loss between the temperature 50 °C and 750 °C (inset graph). The weight loss is about 10% due to combustion of polymer in the structure of nanocomposite. TG analysis showed the presence of 10% PPyAA around 90% magnetic core (Fe_3O_4).

3.5. Magnetization

M–H hysteresis curves of bulk magnetite and PPyAA–Fe_3O_4 nanocomposite, measured at room temperature, are shown in Fig. 5. It was observed that both composite and the bulk material do not reach to saturation at high fields up to 15 kOe. Besides, there is no measurable coercivity in either of the samples.

The specific saturation magnetization (M_S) of the samples is determined from M versus $1/H$ curves (M at $1/H \geq 0$) as 63.5 emu/g and 13 emu/g for the bulk and composite, respectively. Here, we should note that magnetization of the composite sample should be normalized to the mass of the magnetic core. According to the TGA histogram of the composite sample, nearly 90% of the total mass corresponds to that of the magnetite. Therefore, normalized saturation magnetization of the composite becomes 21.7 emu/g that is still far from the theoretically determined magnetization of bulk magnetite that is 92 emu/g [1,37]. Thus, above observations imply that Fig. 5. reveals characteristic feature behavior of superparamagnetic (SP) particles with grain sizes smaller than 20 nm.

Reduced magnetization is often observed in SP magnetite particles [2,12,38–40] and explained by spin canting and presence of disordered spins at the surface [2,12,36,39,40]. As particle size decreases, effect of surface spins to the overall magnetization increases due to the presence of a considerably high fraction of all spins on the surface. In addition to spin canting and presence of disordered spins at the surface, adsorption of surfactant molecules to the surface of magnetite particles can be another reason of the low magnetization values in the nanocomposites. We have observed in our previous works [2,12,41] and in this study, surfactant molecules are bound to the surface over oxygen atoms that is revealed from the FT-IR analysis results. As a result, the super-exchange interaction between Fe and O atoms (Fe–O) (superexchange (or Kramers–Anderson superexchange) is the strong (usually) antiferromagnetic coupling between two next-to-nearest neighbor Fe cations through a non-magnetic anion (O^{2-})) gets weaker because of some spins of the pinned oxygen atoms which are close to the surface (i.e., their contribution to the magnetization is cancelled). Then, overall magnetization of the nanocomposite decreases.

Room temperature magnetization curves can be used to calculate average particle size of the nanocomposites with an assumption that they are weakly or non-interacting SP particles. Langevin function, which describes the magnetization of SP particles, should be fit to the measured *M–H* hysteresis curves. Theoretical fitting gives us mean magnetic moment (μ) of particles that is used to determine average particle size (D) using the relation $\mu = M_S \pi \rho D^3/6$. In this way, we have determined mean magnetic moment of the bulk magnetite as $9.856 \mu_B$ that gives the average particle size of this material as 8.23 ± 1 nm. This estimated magnetic core size is smaller than the crystallite size which confirms the presence of magnetically dead layers on the nanoparticles due to nanocomposite formation.

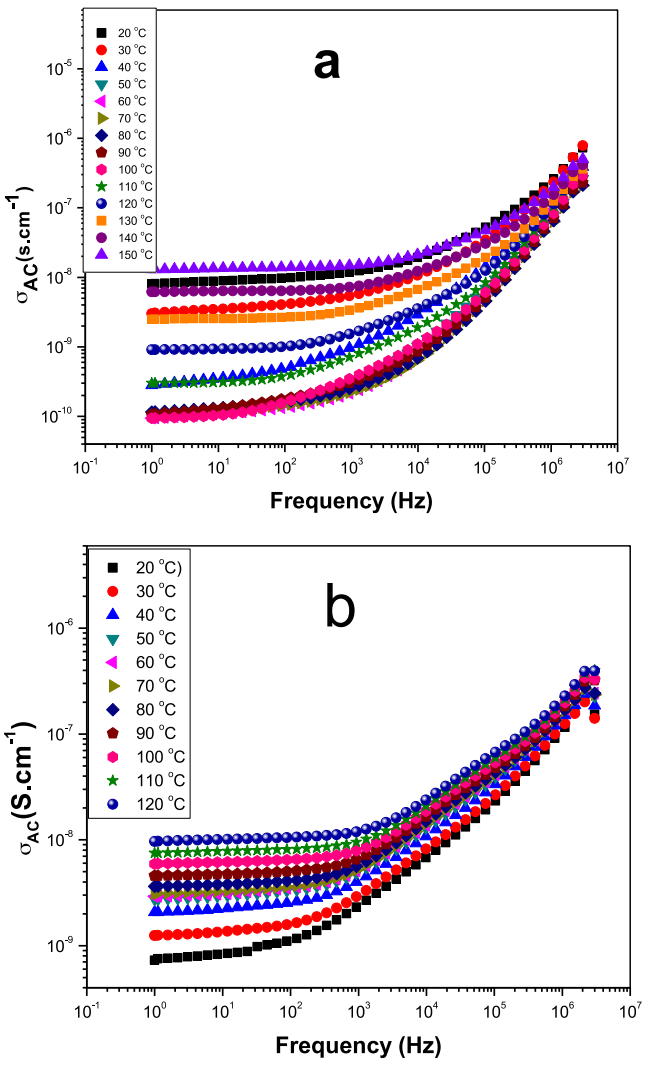

Fig. 6. The variation of a.c. conductivity of (a) PPyAA–Fe_3O_4 nanocomposite and (b) pristine PPyAA as a function of frequency and temperature.

3.6. Temperature and frequency dependent conductivity and dielectric permittivity measurements

The frequency and temperature dependent alternating current (a.c.), direct current (d.c.) conductivity and dielectric permittivity properties of both pristine poly[1-(2-carboxyethyl)pyrrole] (PPyAA) and PPyAA–Fe_3O_4 nanocomposite are discussed here and the related figures were given in the following sections in detail.

3.6.1. a.c. conductivity

The a.c. conductivity of PPyAA–Fe_3O_4 nanocomposites was measured from 20 up to 150 °C using impedance spectroscopy while the conductivity of pristine PPyAA was evaluated in the range of 20–120 °C. a.c. conductivities of the samples were obtained using the following standard equation [13,42]

$$\sigma_{a.c.}(\omega) = \varepsilon''(\omega)\omega\varepsilon_0 \quad (1)$$

where $\sigma_{a.c.}(\omega)$ is the real part of conductivity, $\omega(2\pi f)$ is the angular frequency of the signal applied to the sample, ε'' is the imaginary part of complex dielectric permittivity and ε_0 (8.852×10^{-14} F cm^{-1}) is the vacuum permittivity. The frequency and temperature dependent a.c. conductivity graphs of PPyAA–Fe_3O_4 and pristine PPyAA are shown in Fig. 6(a) and (b), respectively. a.c. conductivities of PPyAA–Fe_3O_4 nanocomposite at 1 Hz are found to be 8.26×10^{-9} and 1.44×10^{-8} S cm^{-1} for 20 and 150 °C, respectively while a.c. conductivity of PPyAA was 9.89×10^{-9} S cm^{-1} at 120 °C. Interestingly, the a.c. conductivity of the nanocomposite slightly decreases with temperature up to 100 °C. Beyond this temperature, the conductivity of PPyAA–Fe_3O_4 nanocomposite raised again to the level of conductivity observed at 20 °C whereas the conductivity of pristine PPyAA slightly and steadily increased with temperature. This divergence observed in the conductivity of nanocomposite can be explained as follows: At low temperature, magnetite nanoparticles surrounded by PPyAA can form a random network. When the temperature is increased, the nanocomposite consisting of magnetite becomes more organized and exhibits more capacitive behavior. This situation results in high electrical conductivity.

Regarding the temperature dependency of a.c. conductivity, both PPyAA–Fe_3O_4 nanocomposite and pristine PPyAA showed temperature dependent and temperature independent behaviors (a dispersive regime) at low and high frequencies, respectively (Fig. 6(a) and (b)). This phenomenon is a strong clue for ionic conductivity [12,18]. The ionic hopping in iron oxide occurs between Fe^{2+} and Fe^{3+} sites [43–46]. On the other hand, the charge transfer in PPyAA occurs between the polaron and bipolaron states [47]. In this process, mobility of the charge carrier increases with temperature which results in a significant reduction in d.c. resistivity. In particular, the ionic or vacant sites cause a limitation in the mobility of charge carriers and this leads to a minor effect of charge transfer on the conduction properties of nanocomposite [16]. Therefore, it is concluded that hopping process is the major type of conduction.

The conductivity of nanocomposite was slightly lower than that of pristine PPyAA since the interactions between the polymer matrix and iron oxide nanoparticles will increase the charge carrier scattering and thus increase the sample resistivity when Fe_3O_4 nanoparticles were embedded into PPyAA matrix. Other effects like increased carrier charge trapping either by the nanoparticles themselves or by morphological changes, could also play a role in slight reduction of conductivity [48]. Contrarily, the electrically conductive ferromagnetic nanocomposites were described formerly in literature [49,50]. In other words it was reported the conductivity of magnetite including sulfone polyaniline (sPANi) nanocomposite had higher values than that of pristine PANi and sPANi [50] and this result was attributed to the changes in micro- and macroscopic factors such as crystalline size and morphology of polymer after adding Fe_3O_4 particles into the polymer matrix.

Concerning the frequency dependency of a.c. conductivity of nanocomposite and pristine PPyAA, they exhibited nearly the same frequency dependent behavior. Apart from each other, the a.c. conductivity of nanocomposite changed with frequency beyond 100 kHz while pristine PPyAA had frequency dependent conductivity properties above 10 kHz. At high frequencies, a.c. conductivity of each product varied with the same way but independent of temperature. In other word, a.c. conductivity over a certain frequency (100 kHz for nanocomposite and 10 kHz for pristine PPyAA) obeyed the rule of the temperature independent expression for several low mobility polymers and even for crystalline materials, non-crystalline and liquid semiconductors;

$$\sigma_{a.c.}(\omega) = A\omega^n \quad (2)$$

where ω is the angular frequency, n is the frequency exponent and A is a temperature independent constant [51,52]. Frequency exponent (n) values were calculated from the slopes of log–log graph and the figures are shown in Fig. 7. By fitting our data to Eq. (2), we found n values of about 0.5 and in the range of 0.8–1.2 for pristine PPyAA and nanocomposite (inset of Fig. 7(a) and (b)), respectively. The obtained n results showed us that the a.c. conductivity of each sample is dependent of temperature.

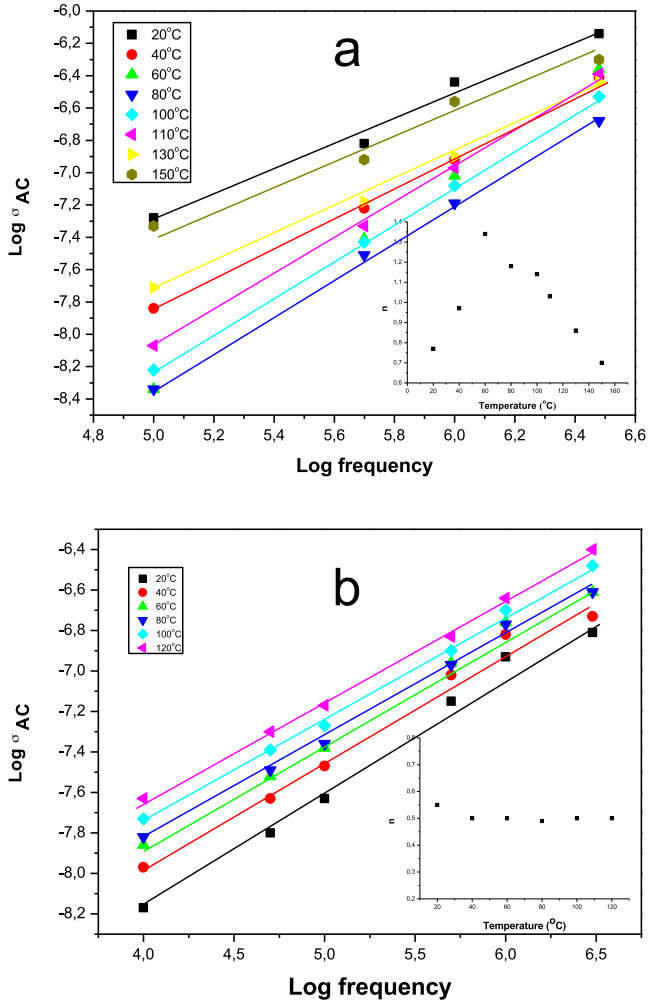

Fig. 7. Plots of $\log \sigma_{a.c.}$ versus $\log \omega_{max}$ and n versus inverse absolute temperature of (a) PPyAA–Fe_3O_4 nanocomposite and (b) pristine PPyAA.

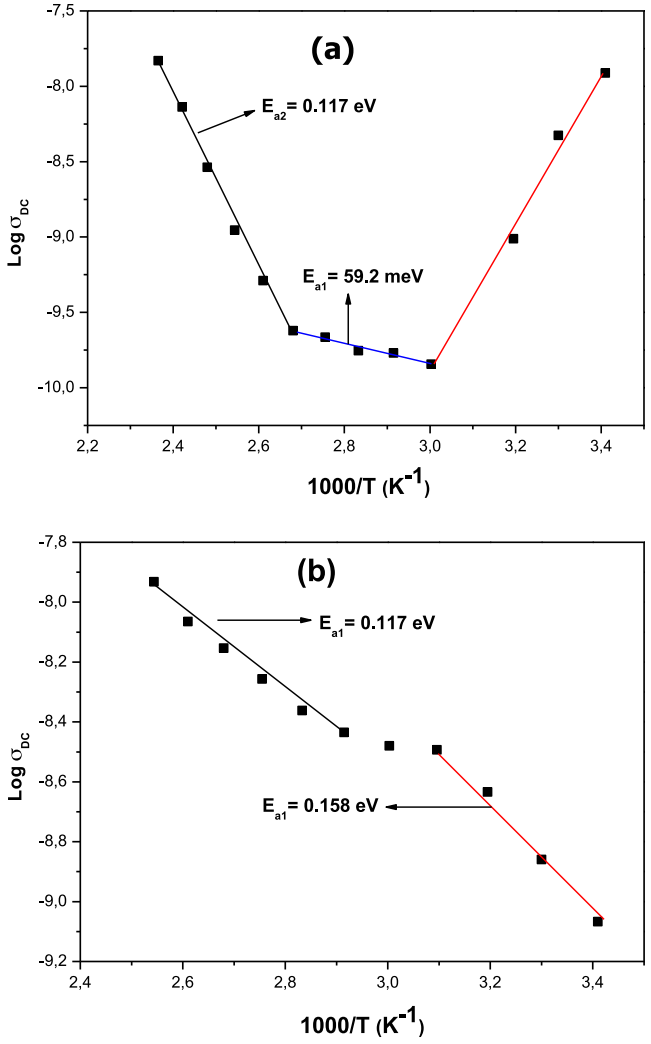

Fig. 8. d.c. conductivity of (a) PPyAA–Fe_3O_4 nanocomposite and (b) pristine PPyAA versus reciprocal temperature.

Additionally, the variation of n values of PPyAA–Fe_3O_4 nanocomposite with temperature is a strong evidence for thermally activated polarization mechanism whereas the polarization mechanism of pristine PPyAA cannot be considered thermally activated due to unchanged n value. On the other hand, if we assume that the conduction mechanism is based on ion migration in the applied electric field, the lower s values from the a.c. measurements can be explained by strong electrode polarization. In addition, a.c. conductivity of the nanocomposite showed a linear increase in the log–log plot (power law behavior) due to the increase of conductivity of the PPyAA–Fe_3O_4 nanocomposites above 60 °C while substantial changes at low frequency were only found at lower temperatures than this temperature as seen in Fig. 7.

3.6.2. d.c. conductivity

The direct current (d.c.) conductivity of the nanocomposite and pristine PPyAA was derived from the plateau regions presented in Fig. 6 and the d.c. conductivity of PPyAA–Fe_3O_4 nanocomposite versus reciprocal temperature is depicted in Fig. 8(a) with the illustration of linear fittings and transition regions. The curve demonstrated that d.c. strongly depended on temperature together with two characteristic transitions. Specifically, magnetite-capped systems exhibit Arrhenius behavior at various temperature ranges, providing three values of the activation energy below and above first temperature transition of around 60 °C and second temperature transition of above 100 °C. One can see from Fig. 8(a) that the d.c. conductivity of nanocomposite was found to obey thermally activated Arrhenius plot conduction of

$$log\, \sigma_{d.c.} = \log\, \sigma_0 - \frac{E_a}{k_B T} \quad (3)$$

where $\sigma_{d.c.}$ is the d.c. conductivity, E_a is the activation energy, k_B is the Boltzmann constant (8.617 eV K^{-1}) and T is the temperature in K. Subsequently E_a values were found to be 117 meV and 59.2 meV for nanocomposite while two different activation energies were calculated as 0.158 eV and 0.117 eV for pristine PPyAA.

d.c. conductivity of PPyAA–Fe_3O_4 nanocomposite can be classified into three regions up to 150 °C. While first transition temperature between RT and 60 °C demonstrated a decrease in the electrical conductivity, higher temperatures above 60 °C lead to an increase of electrical conductivity due to semiconducting nature of ferrite. The second transition temperature above 100 °C caused a remarkable increase in the conductivity. Consequently, it can be emphasized that this phenomenal behavior shows a kind of temperature dependent reorganization of PPyAA–Fe_3O_4 nanocomposite within a certain range of phase transition in nanocomposite structure.

The d.c. conductivity of pristine PPyAA is depicted in Fig. 8(b). The activation energies were calculated as 0.158 eV and 0.117 eV below and above 60 °C, respectively. The reason of the change in activation energy at this temperature may be attributed to

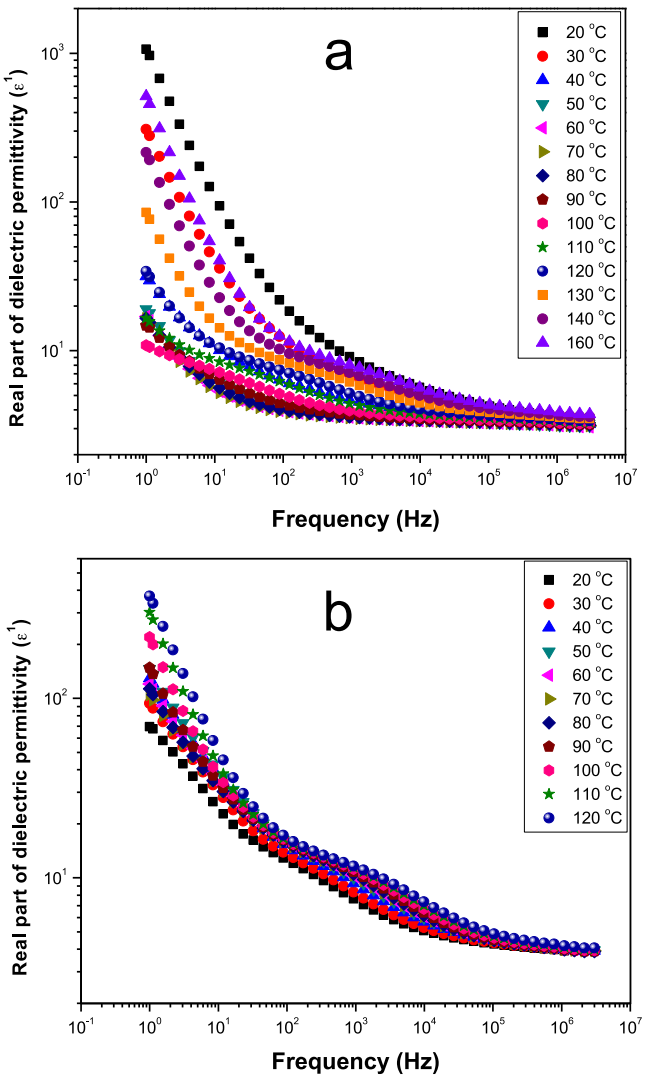

Fig. 9. The variation of real part of dielectric permittivity (ε'): (a) PPyAA–Fe_3O_4 nanocomposite and (b) pure PPyAA depending on temperature and frequency.

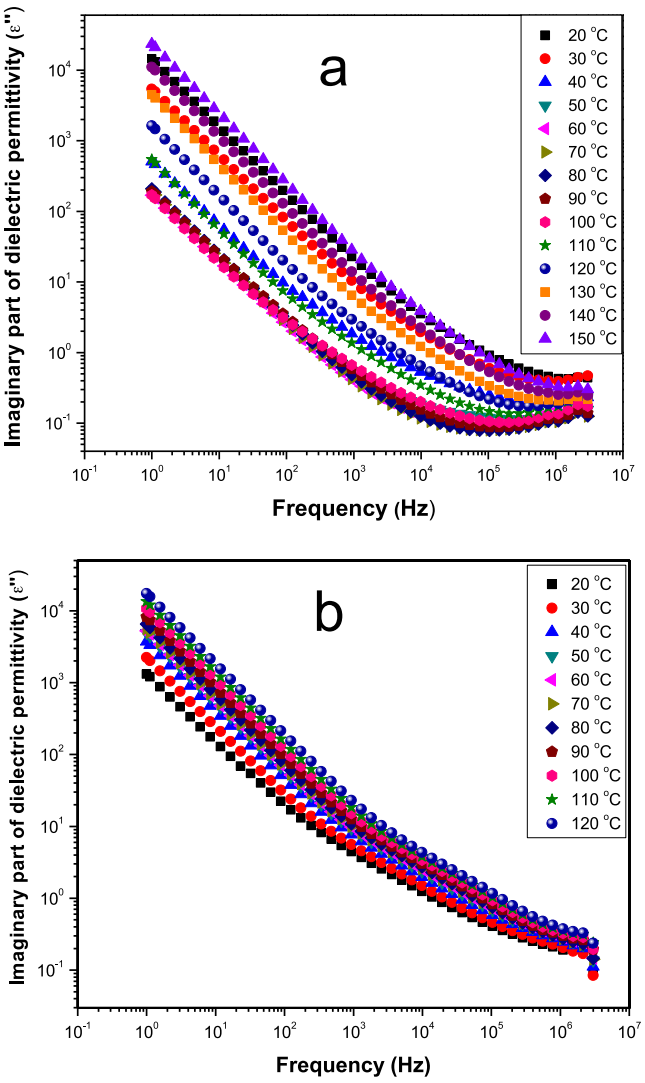

Fig. 10. The variation of imaginary part of dielectric permittivity (ε''): (a) PPyAA–Fe_3O_4 nanocomposite and (b) pure PPyAA as a function of temperature and frequency.

segmental molecular motions of polymer. Similarly, one can see from Fig. 8(b) that the d.c. conductivity of pristine PPyAA was found to obey thermally activated Arrhenius equation given as above.

3.6.3. *Frequency and temperature dependence of dielectric permittivity*

3.6.3.1. Real part of dielectric permittivity. The real part of the complex permittivity (ε') variations of both pristine PPyAA and Fe_3O_4 containing nanocomposite in the frequency range of 1 Hz–3 MHz and temperature range of 20–150 °C are given in Fig. 9(a) and (b). The real part of dielectric permittivity (ε'), which is related to the stored energy within the medium, of each product sharply decreased with frequency and remained almost unchanged at higher frequencies (beyond 15 kHz) when temperature was kept constant. Furthermore, these curves keep their shapes but slide up at higher temperatures. Actually, this decrease in the real part of dielectric permittivity was significant at higher temperature (above 110 °C) for nanocomposite while this attitude was clearly observed in the range of 20–120 °C for pristine PPyAA. Dielectric constants of polymers, in general, are known to decrease gradually with increasing frequency and similar behavior was observed for Fe_3O_4 containing nanocomposite. This behavior can be attributed to the frequency dependence of the polarization mechanisms. The dielectric constant depends upon the ability of the polarizable units in a polymer to orient fast enough to keep up with the oscillations of an alternating electric field. When frequency increases the orientational polarization decreases since the orientation of dipole moments needs a longer time than electronic and ionic polarizations. This causes the dielectric constant to decrease. On the other hand, the increase of ε' towards the low frequency region is also seen from Fig. 9(a) and (b). This may be attributed to the blocking of charge carriers at the electrodes. Furthermore, the variation of relative dielectric constant with frequency also shows the presence of material–electrode interface polarization processes which take place at low frequencies.

Concerning the temperature dependence of the real part of dielectric permittivity, it is clear that ε' increases continuously with increasing temperature for pristine PPyAA. However, the variation of dielectric permittivity of nanocomposite depending on temperature showed us two different behaviors due to the transition temperature of electronically conducting polymer matrix. The expansion of pristine electronically conducting PPyAA matrix can separate the filling components of the nanocomposites that connected with each other earlier when the temperature was lowered. Hence, this yields a reduction in dielectric permittivity until 100 °C. By increase in temperature, the interfaces between Fe_3O_4

and polymer matrix will enhance, and the dielectric constant will rise due to the interfacial polarization [12]. Also with increasing temperature, the thermal energy converts the bound charges to the charge carriers, and the increasing number of charge carriers yields a rising in dielectric constants. Furthermore, the mobility of the charge carriers increases by increasing the temperature because of the increase in thermal energy [13]. On the other hand, it is known from literature that the addition of nanoparticles alters the molecular dynamics of the matrix polymer at low temperatures [52]. This effect is due to the modified interactions at the interfaces between particles and the matrix. The measured effective permittivity depends both on the microstructure and on the permittivity of the nanoparticles [53]. Additionally, this situation can be explained by Clausius–Mosotti equation which explains the relation between dielectric constant of a substance and polarizability coefficient of its dipoles. Thus, the reduction polarization with declining temperature resulted in a significant lowering in dielectric permittivity of both samples.

3.6.3.2. Imaginary part of dielectric permittivity (ε''). Fig. 10(a) and (b) shows the frequency dependence of imaginary part of dielectric permittivity (dielectric loss (ε'')) at different temperatures for PPyAA and PPyAA–Fe_3O_4 nanocomposites. It was observed that imaginary part of dielectric permittivity continuously decreased with frequency and reached a minimum at 20–150 °C temperature interval for nanocomposite. These results for both real and imaginary parts of the permittivity are strongly attributed to the ionic relaxations of the dipoles although dipolar contributions also exist at high frequency region. Regarding the polarization mechanism, it can be emphasized that interface polarization is dominant at lower frequencies while other mechanisms such as electronic and ionic exist at higher frequencies [54]. At high frequency, the imaginary part of permittivity becomes less sensitive to both frequency and temperature, tended to be stabilized as reported earlier [55]. On the other hand, no maximum peak attributed to the relaxation of each samples measured at studied temperature interval. This is probably due to the being out of frequency and temperature range applied in the study.

4. Conclusions

In this study, PPyAA–Fe_3O_4 nanocomposite was synthesized by cooprecipitation and reflux methods. In this work, the a.c. conductivity and dielectric properties of pristine poly 3-pyrrolyl acetic acid and its nanocomposite with Fe_3O_4 are studied in the range of 1–3 MHz frequency range and 20–120 °C temperature interval. The frequency dependence of the a.c. conductivity of nanocomposite obeys the universal power law with a deviation at low temperature and frequency for nanocomposites while no divergence was observed at these conditions for pristine PPyAA. It is clearly emphasized that the conductivity and dielectric permittivity measurements strongly depend on the thermally activated polarization mechanism and thermal transition of PPyAA in the nanocomposite structure. This situation was briefly observed from the d.c. conductivity and dielectric permittivity plots above 60 and 100 °C with two transition peaks for both nanocomposite and pristine PPyAA. The d.c. conductivity of nanocomposite and pristine PPyAA at low and high temperatures can generally be fitted with Arrhenius equation with different E_a values of 117 meV and 59.2 meV. Dielectric permittivity results point out that ionic and polymer segmental motions are strongly coupled with d.c. electrical conductivity which is strongly temperature dependent and can be classified into three regions from 20 to 150 °C for PPyAA–Fe_3O_4 nanocomposite while pristine PPyAA had two different regions. Furthermore, the large value of dielectric permittivity (ε') at lower frequency is attributed to the predominance of species like Fe^{2+} ions and grain boundary defects (interfacial polarization).

Acknowledgements

The authors are thankful to the Fatih University, Research Project Foundation (Contract no: P50020902-2) and TUBITAK (Contract no: 110T487) for financial support of this study.

Appendix A. Supplementary data

Supplementary data associated with this article can be found, in the online version, at doi:10.1016/j.jallcom.2011.06.002.

References

[1] J.O. Parka, K.Y. Rheeb, S.J. Park, Appl. Surf. Sci. 256 (2010) 6945.
[2] Z. Durmus, H. Erdemi, A. Aslan, M.S. Toprak, H. Sozeri, A. Baykal, Polyhedron 30 (2011) 419–426.
[3] X. Lu, W. Zhang, C. Wang, T.C. Wen, Y. Wei, Prog. Polym. Sci. 36 (2011) 671.
[4] H. Gómez, M.K. Ram, F. Alvi, P. Villalba, E. Stefanakos, A. Kumar, J. Power Sources 196 (2011) 4102.
[5] T. Rajesh, D. Ahuja, D. Kumar, Sens. Actuators B 136 (2009) 275.
[6] S. Jafarzadeh, A. Adhikari, P.E. Sundall, J. Pan, Prog. Org. Coat. 70 (2011) 108.
[7] Z. He, Y. Fang, X. Wang, H. Pang, Synth. Met. 161 (2011) 420.
[8] J. Jiang, C. Chen, L.-H. Ai, L.C. Li, H. Liu, Mater. Lett. 63 (2009) 560.
[9] Y. Wang, L. Li, J. Jiang, H. Liu, H. Qiu, F. Xu, React. Funct. Polym. 68 (2008) 1587.
[10] S.A. Saafan, T.M. Meaz, E.H. El-Ghazzawy, J. Magn. Magn. Mater. 323 (2011) 1517.
[11] J. Meng, C. Shi, B. Wei, W. Yu, C. Deng, X. Zhang, J. Chromatogr. A 1218 (2011) 2841.
[12] B. Ünal, Z. Durmus, A. Baykal, H. Sözeri, M.S. Toprak, L. Alpsoy, J. Alloys Compd. 505 (2010) 172.
[13] B. Unal, Z. Durmus, H. Kavas, A. Baykal, M.S. Toprak, Mater. Chem. Phys. 123 (2010) 184.
[14] Z. Durmus, H. Kavas, M.S. Toprak, A. Baykal, T.G. Altınçekiç, A. Aslan, A. Bozkurt, S. Coşgun, J. Alloys Compd. 484 (2009) 371.
[15] M. Aydın, Z. Durmus, H. Kavas, B. Esat, H. Sözeri, A. Baykal, F. Yılmaz, M.S. Toprak, Polyhedron 30 (2011) 1120.
[16] H. Kavas, Z. Durmus, A. Baykal, A. Aslan, A. Bozkurt, M.S. Toprak, J. Noncryst. Solids 356 (2010) 484.
[17] B. Birsöz, A. Baykal, H. Sözeri, M.S. Toprak, J. Alloys Compd. 493 (2010) 481.
[18] A. Baykal, N. Bıtrak, B. Ünal, H. Kavas, Z. Durmus, Ş. Özden, M.S. Toprak, J. Alloys Compd. 502 (2010) 199.
[19] Y. Köseoğlu, A. Baykal, F. Gözüak, H. Kavas, Polyhedron 28 (2009) 2887.
[20] H. Kavas, A. Baykal, M.S. Toprak, Y. Köseoğlu, M. Sertkol, B. Aktaş, J. Alloys Compd. 479 (2009) 49.
[21] C. Li, G. Shi, Electrochim. Acta (2011), doi:10.1016/j.electacta.2010.12.081.
[22] A.A. Farghali, M. Moussa, M.H. Khedr, J. Alloys Compd. 499 (2010) 98.
[23] B. Unal, Z. Durmus, A. Baykal, M.S. Toprak, H. Sozeri, A. Bozkurt, J. Alloys Compd. (2010), doi:10.1016/j.jallcom.2011.05.001.
[24] X. Liang, Z. Wen, Y. Liu, X. Wang, H. Zhang, M. Wu, L. Huang, Solid State Ionics (2010), doi:10.1016/j.ssi.2010.07.016.
[25] A.A. Khan, L. Paquiza, Synth. Met. 161 (2011) 899.
[26] S.H. Hosseini, S.H. Mohseni, A. Asadnia, H. Kerdari, J. Alloys Compd. 509 (2011) 4682.
[27] J. Jiang, L. Ai, L. Li, J. Phys. Chem. B 113 (2009) 1376.
[28] L.H. Ai, J. Jiang, J. Alloys Compd. 487 (2009) 735.
[29] T. Özkaya, M.S. Toprak, A. Baykal, H. Kavas, Y. Köseoğlu, B. Aktaş, J. Alloys Compd. 472 (2009) 18.
[30] L. Zhang, R. He, H.C. Gu, Appl. Surf. Sci. 253 (2006) 2611.
[31] V.P. Kurikka, M. Shafi, A. Ulman, X. Yan, N.L. Yang, C. Estournés, H. White, M. Rafailovich, Langmuir 17 (2001) 5093.
[32] L.J. Kirwan, P.D. Fawell, W.V. Bronswijk, Langmuir 19 (2003) 5802.
[33] F. Jones, J.B. Farrow, W. van Bronswijk, Langmuir 17 (1998) 6512.
[34] T. Wejrzanowski, R. Pielaszek, A. Opalinska, H. Matysiak, W. Łojkowski, K.J. Kurzydłowski, Appl. Surf. Sci. 253 (2006) 204.
[35] R. Pielaszek, Appl. Crystallography, Proceedings of the XIX Conference, Kraków, Poland, September, 2003, p. 43.
[36] A.E. Berkowitz, J.A. Lahut, I.S. Jacobs, L.M. Levinson, D.W. Forester, Phys. Rev. Lett. 34 (1975) 594.
[37] B.D. Cullity, Introduction to magnetic materials, vol. 61, Addison-Wesley, Reading, MA, 1972, p. 190.
[38] J. Mürbe, A. Rechtenbach, T. Töpfer, Mater. Chem. Phys. 110 (2008) 426.
[39] R.H. Kodama, A.E. Berkowitz, E.J. McNiff Jr., S. Foner, Phys. Rev. Lett. 77 (1996) 394.
[40] X. Batlle, A. Labarta, J. Phys. D: Appl. Phys. 35 (2002) R15.
[41] Z. Durmus, H. Sözeri, B. Unal, A. Baykal, R. Topkaya, S. Kazan, M.S. Toprak, Polyhedron 30 (2011) 322.
[42] S.U. Celik, A. Bozkurt, Eur. Polym. J. 44 (2008) 213.

[43] A.C.V. Araujo, R.J. Oliveira, S.A. Junior, A.R. Rodrigues, F.L.A. Machado, F.A.O. Cabral, W.M. Azevedo, Synth. Met. 160 (2010) 685.
[44] J.C. Dyre, J. Appl. Phys. 64 (1988) 2456.
[45] I.H. Gul, A.Z. Abbasi, F. Amin, M. Anis-ur-Rehman, A. Maqsood, J. Magn. Magn. Mater. 311 (2007) 494.
[46] G.C. Psarras, Composites A 37 (2006) 1545–1553.
[47] G.G. Wallace, G.M. Spinks, L.A.P. Kane-Maquire, P.R. Teasdale, Conductive Electroactive Polymers – Intelligent Materials Systems, CRC Press, 2003, ISBN 1-58716-127-3.
[48] Y. Longa, Z. Chena, J. Duvail, Z. Zhang, M. Wan, Physica B 370 (2005) 121.
[49] A.C.V. de Araujo, R.J. de Oliveira, S.A. Junior, A.R. Rodrigues, F.L.A. Machado, F.A.O. Cabral, W.M. de Azevedo, Synth. Met. 160 (2010) 685.
[50] K.R. Reddy, K.P. Lee, A.I. Gopalan, J. Appl. Polym. Sci. 106 (2007) 1181.
[51] N.F. Mott, E.A. Davis, Electronic Processes in Non-crystalline, Clarendon Press, Oxford, 1971–1979.
[52] H. Deligöz, S. Özgümüş, T. Yalçınyuva, S. Yıldırım, D. Değer, K. Ulutaş, Polymer 46 (2005) 3720.
[53] X. Pan, H. Shen, J. Qiu, M. Gu, Mater. Chem. Phys. 101 (2007) 505.
[54] D. Değer ve, H.K. Ulutaş, Vacuum 72 (2004) 307.
[55] Y. Köseoğlu, M. Bay, M. Tan, A. Baykal, H. Sözeri, R. Topkaya, N. Akdoğan, J. Nanopart. Res. 13 (2011) 2235.